J Adv Ceram

Research Article

Achieving superior strength-toughness synergy in ZrC-based ceramics: An *in situ* multiscale construction strategy via a two-step reactive SPS process

Boxin Wei[1,✉], Zhichao Zhuang[1], Yang Yang[1], Dong Wang[2], Lei Chen[3], Yujin Wang[3,✉]

Cite this article: Wei B, Zhuang Z, Yang Y, et al. *J Adv Ceram* 2026, **15**(4): 9221263. https://doi.org/10.26599/JAC.2026.9221263

ABSTRACT: To overcome the poor sinterability and low fracture toughness (K_{IC}) of zirconium carbide (ZrC) ceramics, a novel multiscale microstructure design was proposed via a two-step *in situ* reactive spark plasma sintering (SPS) process using ZrC, $TiSi_2$, and B_4C powders. During sintering, $TiSi_2$ preferentially reacted with B_4C to form TiB_2 and primary silicon carbide (SiC), while the released Si further reacted with ZrC to yield $ZrSi_2$ and secondary SiC. The two-step SPS (1600 °C/3 min + 1800 °C/10 min) promoted complete *in situ* reactions, liquid-phase sintering, and interdiffusion of Zr/Ti, leading to the formation of (Zr,Ti)C and (Ti,Zr)B_2 solid solutions. With the addition of 30 mol% $TiSi_2$ and 15 mol% B_4C, the multiphase ceramics exhibited a refined submicrostructure (grain size < 500 nm), achieving a high flexural strength of 824±46 MPa and K_{IC} of 7.5±0.5 MPa·m$^{1/2}$. The synergistic enhancement in strength and toughness is attributed to a multiscale strengthening/toughening mechanism: solid-solution strengthening at the atomic scale, effective grain boundary pinning by nanosized primary and secondary SiC particles at the nanoscale, and toughening through crack deflection and bridging by TiB_2–SiC agglomerates and the higher-toughness $ZrSi_2$ phase at the microscale. This work provides a viable and innovative approach for designing high-performance ultrahigh-temperature ceramics through tailored *in situ* reactions and microstructural control.

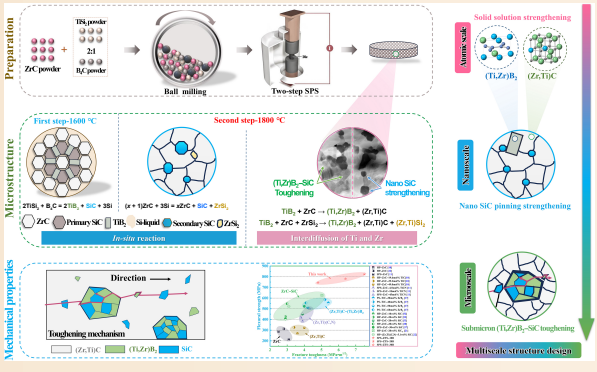

KEYWORDS: zirconium carbide (ZrC); spark plasma sintering (SPS); *in situ* reaction; multiscale microstructure; mechanical properties

1 Introduction

Zirconium carbide (ZrC) is characterized by a high melting point (~3420 °C), low density (6.73 g/cm^3), and high hardness (~26 GPa), along with good thermal shock resistance and solid-state stability. These properties render it a promising candidate for ultrahigh-temperature applications, including components in engine propulsion systems, nose caps of hypersonic vehicles, and leading edges [1,2]. Moreover, owing to its remarkable resistance to fission product corrosion and irradiation damage, ZrC has been regarded as a potential material for tri-structural isotropic (TRISO)-coated fuel particles, fuel cladding, and inert matrix fuel (IMF) in Generation-IV nuclear energy systems [3–5]. In the fabrication of IMF, lowering the sintering temperature is essential to prevent reactions between the fuel and the matrix [6]. Nevertheless, the strong covalent bonding and low self-diffusion coefficient of ZrC result in poor sinterability, which limits its broader application [7]. Additionally, the inherent brittleness of ZrC further restricts its use under extreme operating conditions [8]. Therefore, developing a processing strategy that can simultaneously achieve low-temperature densification and construct a toughening architecture remains a critical challenge.

To enhance the sintering performance and improve the strength and toughness of ZrC ceramics, introducing titanium (Ti) from the same group IVB to form (Zr,Ti)C solid solutions is a widely adopted practice [9]. TiC shares the same crystal structure and similar physical properties as ZrC. The resulting solid solution can improve the flexural strength and hardness but exerts a limited effect on toughness [9,10]. In our previous work, we concurrently introduced Ti and N to form an anion-cation costabilized (Zr,Ti)(C,N) solid solution, which increased the flexural strength to 503 MPa and the fracture toughness (K_{IC}) to

[1] School of Materials Science and Chemical Engineering, Harbin University of Science and Technology, Harbin 150040, China. [2] School of Materials Science and Engineering, Anhui University of Technology, Ma'anshan 243002, China. [3] Institute for Advanced Ceramics, School of Materials Science and Engineering, Harbin Institute of Technology, Harbin 150001, China.

✉ Corresponding authors. E-mail: B. Wei, weiboxin@hrbust.edu.cn; Y. Wang, wangyuj@hit.edu.cn

Received: December 7, 2025; Revised: February 7, 2026; Accepted: February 11, 2026

4.3 MPa·m$^{1/2}$ [11]. Furthermore, studies have demonstrated that nitrogen doping significantly reduces the stacking fault (SF) energy of the (Ti,Zr)C system, thereby promoting dislocation emission and multiplication during phase separation. This leads to a synergistic enhancement in both hardness and toughness, with the K_{IC} approaching 3.7 MPa·m$^{1/2}$ [12]. Additionally, nitrogen doping facilitates the formation of Zr–C–N–O oxide network structures at temperatures below the melting point of the oxides, markedly improving the ablation resistance of ZrC ceramics [13]. However, N tends to form N_2 gas during high-temperature sintering, which can hinder the densification process [11]. Another strengthening approach involves the introduction of boron (B). Plate-like TiB_2 can improve the toughness of carbide ceramics [14]. Directly introducing TiB_2 into ZrC promotes densification via Ti/Zr interdiffusion and increases the Vickers hardness (H_v) [15]. In our previous study [16,17], we fabricated (Zr,Ti)C–(Ti,Zr)B_2 solid solution ceramics via the reactive sintering of TiC and ZrB_2. The *in situ* reaction of TiC and ZrB_2 lowered the densification temperature (1750 °C) [16], promoted Zr/Ti interdiffusion, and consequently enhanced both flexural strength (555 MPa) and toughness (5.4 MPa·m$^{1/2}$) [17]. In binary/ternary carbide–diboride systems, this mutual exchange of metal elements is known to enhance densification, improve toughness, and refine the microstructure [18]. Additionally, the introduction of B can also improve the oxidation resistance of carbide ceramics [19]. Therefore, the introduction of TiB_2 proves to be an effective strategy for enhancing both the sinterability and the mechanical properties (strength and toughness) of ZrC ceramics.

The incorporation of silicon carbide (SiC) has also been demonstrated as an effective approach for improving the toughness of ZrC ceramics. For instance, Zhao *et al.* [20] produced ZrC–20 vol% SiC composites by hot pressing with SiC powders of varying particle sizes and found that the composite exhibited higher K_{IC} when the initial SiC particle size was 3.5 μm. In another study, Li *et al.* [21] developed ZrC–20 vol% SiC whisker (SiC_w) composites, which reached a flexural strength of 626.17 MPa and a K_{IC} of 5.03 MPa·m$^{1/2}$. However, the direct addition of SiC does not improve the sinterability of ZrC ceramics, as the densification temperature remains relatively high. In contrast, our previous work demonstrated that introducing Si to react *in situ* with ZrC can markedly lower the sintering temperature while increasing the flexural strength (up to 522 MPa) [22]. The use of low-melting-point Si/silicides promotes densification, and the *in situ* formed SiC particles, which are notably finer, exert a physical pinning effect that further enhances strength. Moreover, the incorporation of SiC also improves the oxidation resistance of ZrC ceramics [23].

Based on the foregoing analysis, to achieve a synergistic improvement in the sinterability, strength, and toughness of ZrC ceramics, a combined introduction of TiB_2 and SiC is considered an effective approach. However, to realize a breakthrough in the strength of ZrC-based ceramics, further grain refinement toward a nanostructured microstructure is essential. This can be accomplished by leveraging *in situ* reactions, where renucleation effectively reduces the grain size and refines the microstructure. Consequently, this study utilizes the *in situ* reaction between $TiSi_2$ and B_4C to generate TiB_2 and SiC ($2TiSi_2 + B_4C \rightarrow 2TiB_2 + SiC + 3Si$). The *in situ* formation of TiB_2 + SiC via $TiSi_2$ addition has proven to be an effective toughening strategy in B_4C-based ceramics, achieving K_{IC} values exceeding 6 MPa·m$^{1/2}$ [24,25]. The reaction between $TiSi_2$ and B_4C initiates at approximately 1000 °C [24]. Furthermore, to control the grain size and achieve microstructural refinement, a two-step spark plasma sintering (SPS) process was employed to fabricate ZrC-based ceramics. SPS provides an effective strategy to activate the sintering kinetics of challenging materials, including nanostructured systems, leading to comprehensive property improvements [26]. Compared with conventional sintering methods, SPS enables rapid heating and full densification at lower temperatures and within shorter durations [27]. Additionally, studies indicate that the electric field applied during SPS improves the wettability of the liquid phase, thereby enhancing densification in the initial sintering stages [28]. In the two-step SPS process, the lower-temperature hold prioritizes the completion of the *in situ* reactions, generating a high density of fine TiB_2 and SiC nuclei while intentionally limiting overall matrix grain growth and densification. With the pinning phases already preformed and dispersed, this subsequent high-temperature rapid sintering achieves full density. Crucially, the preexisting nanoscale particles now effectively pin grain boundaries from the outset, dramatically suppressing coarsening during final densification.

In this study, a novel "thermodynamically driven, kinetically controlled" strategy is proposed to fabricate ZrC-based multiphase ceramics with a hierarchical architecture. A multiscale microstructure design was implemented to fabricate ZrC-based ceramics via a two-step *in situ* reactive SPS process using ZrC, $TiSi_2$, and B_4C powders as raw materials. The molar ratio of $TiSi_2$ to B_4C was fixed at 2 : 1, and the $TiSi_2$ addition was varied at 10, 20, and 30 mol%. The effect of $TiSi_2$ and B_4C addition on the microstructures and mechanical properties was systematically investigated. This work offers critical insights into designing and strengthening/toughening ultrahigh-temperature carbide ceramics via tailored phase and microstructural control.

2 Materials and methods

2.1 Materials preparation

The raw materials consisted of nano-sized ZrC powders (particle size 0.17–0.32 μm, purity > 99.5 wt%, supplied by Changyu Advanced Materials Co., Ltd., China), commercial $TiSi_2$ powders (particle size 1 μm, purity > 99%, Hunan Huawei Aerospace Special Materials Co., Ltd., China), and B_4C powders (particle size 1 μm, purity 98%, Jingangzuan Boron Carbide Co., Ltd., China). According to the *in situ* reaction $2TiSi_2 + B_4C \rightarrow 2TiB_2 + SiC + 3Si$, a reinforcing unit with a fixed $TiSi_2$: B_4C molar ratio of 2 : 1 was introduced into ZrC. The $TiSi_2$ addition was varied as 10, 20, and 30 mol%, corresponding to B_4C contents of 5, 10, and 15 mol%, respectively. For simplicity, the resulting multiphase ceramics are labeled ZTS-10B, ZTS-20B, and ZTS-30B according to the $TiSi_2$ addition. The powder blends with different ZrC/$TiSi_2$/B_4C ratios were homogenized via two-dimensional planetary ball milling using silicon nitride grinding media. The milling was performed at a ball-to-powder mass ratio of 5 : 1 and a rotational speed of 150 r/min for 12 h. Afterwards, the milled powders were sieved through a 200-mesh screen to reduce agglomeration. The mixed powders were compacted in a high-strength graphite mold with an inner diameter of 40 mm and sintered in a pulsed-current spark-plasma sintering furnace (SPS-10T-10-IV, Shanghai Chenhua Electric Furnace Co., Ltd., China) under a dynamic vacuum below 10 Pa. A two-step reactive SPS schedule was applied: The sample was first held at 1600 °C for 3 min, then at 1800 °C for 10 min, with a constant heating rate of 100 °C/min. The 1600 °C step is designed to be reaction-dominated, efficiently creating the desired reinforcing phases and a liquid to boost densification. The 1800 °C step is diffusion-dominated and

optimized to facilitate solid solution formation, which enhances the mechanical properties. A uniaxial pressure of 40 MPa was gradually applied upon reaching 1600 °C. Temperature, time, punch displacement, and pressure were recorded by the SPS system. In addition, for comparison purposes, we also designed a one-step sintering process. The detailed composition design and sintering parameters are summarized in Table 1.

2.2 Materials characterization

Thermodynamic calculations were performed with HSC Chemistry 6.0 and FactSage 7.1. Phase identification was conducted via an X-ray diffractometer (XRD; X'Pert PRO, PANalytical, the Netherlands) using Cu Kα radiation (40 kV/100 mA) in the 2θ range of 10°–90° at a scanning speed of 10 (°)/min. Quantitative phase analysis and lattice-parameter determination were carried out by Rietveld refinement with GSAS-II software. The bulk density was measured based on Archimedes' principle, while the theoretical density was computed from the weighted sum of the densities of individual phases. The relative density (RD) was then obtained from the ratio of these two values. Microstructures were examined using a field-emission scanning electron microscope (FE-SEM; Hitachi SU5000, Hitachi, Japan) on mechanically polished surfaces. Grain sizes were statistically analyzed from at least 50 grains per sample. Nanoscale features were characterized by a scanning transmission electron microscope (STEM; FEI Talos F200X, FEI, USA) in high-angle annular dark-field (HAADF) mode. Mechanical properties were evaluated as follows: Flexural strength (σ) was determined via three-point bending on bars of 3 mm × 4 mm × 24 mm using a universal testing machine (Instron-1186, USA; span 20 mm, crosshead speed 0.5 mm/min), with the reported value being the average of five tests. H_v was measured on polished surfaces under a load of 9.8 N with a dwell time of 10 s, averaging over at least 10 indentations per sample. The elastic modulus (E) was measured by a resonance frequency damping analyzer (RFDA-HTVP-1750C, IMCE, Belgium). The ceramic sample size was 3 mm × 4 mm × 36 mm, and the sample size and mass were measured before testing. K_{IC} was assessed by the single-edge notched beam (SENB) method on notched bars (2 mm × 4 mm × 20 mm, notch width 0.20 mm, depth 2.0 mm) with a span of 16 mm and a crosshead speed of 0.05 mm/min. The K_{IC} of the specimen was calculated according to Eq. (1):

$$K_{IC} = \frac{3PL\sqrt{10a}}{200bh^2}\left(1.93 - 3.07\left(\frac{a}{h}\right) + 14.53\left(\frac{a}{h}\right)^2 - 25.07\left(\frac{a}{h}\right)^3 + 25.80\left(\frac{a}{h}\right)^4\right) \quad (1)$$

where K_{IC} denotes the fracture toughness (MPa·m$^{1/2}$), P is the fracture load (N), L is the span (mm), a is the notch depth (mm), and b and h are the width and height of the specimen (mm), respectively. The reported K_{IC} was the average value of at least five tests for each condition.

3 Results and discussion

3.1 Thermodynamic calculation

To clarify the relationship between reaction products and composition design in the ZrC–$TiSi_2$–B_4C system, the equilibrium phase diagrams of this system at 1000–1800 °C were calculated using FactSage software (Fig. 1). The phase diagram reveals that at both 1600 and 1800 °C, the three ceramics formed the same types of phases: (Zr,Ti)C, (Ti,Zr)B_2, SiC, and liquid phase. The thermodynamic calculations indicate that the liquid phase is (Zr,Ti)Si_2, not elemental Si. The Si produced *in situ* reacts with the ZrC matrix to form $ZrSi_2$, which then dissolves into unreacted $TiSi_2$ to form (Zr,Ti)Si_2. The melting point of $ZrSi_2$ is 1520 °C [29], while that of $TiSi_2$ is 1480 °C [30]. In contrast to pure Si, (Zr,Ti)Si_2 contains Zr and Ti in the liquid, which can facilitate the interdiffusion of Zr/Ti atoms into the carbide and diboride phases, promoting the formation of (Zr,Ti)C and (Ti,Zr)B_2 solid solution.

The thermodynamic evaluations of potential reactions were conducted using HSC 6.0 software, with the results shown in Fig. S1(a) in the Electronic Supplementary Material (ESM). For the reaction between ZrC and $TiSi_2$, regardless of whether the products were $ZrSi_2$ (Eq. (2)) or ZrSi (Eq. (3)), the Gibbs free energy changes (ΔG) values remained positive across 800–2000 °C, indicating no chemical reaction between the matrix ZrC and $TiSi_2$ (Eqs. (2) and (3)):

$$ZrC + TiSi_2 = ZrSi_2 + TiC \quad (2)$$

$$ZrC + 2/3TiSi_2 = ZrSi + 2/3TiC + 1/3SiC \quad (3)$$

Regarding the reaction between ZrC and the additive B4C, Refs. [31,32] confirm that the two react at approximately 1800 °C to form ZrB_2 and C (Eq. (4)):

$$ZrC + 1/2B_4C = ZrB_2 + 3/2C \quad (4)$$

For the reaction between $TiSi_2$ and B_4C, its ΔG values are the lowest among all aforementioned reactions, indicating a greater thermodynamic driving force. Additionally, considering kinetic factors, above 1600 °C, $TiSi_2$ forms a liquid phase, making the $TiSi_2$–B_4C reaction a liquid–solid reaction. This indirectly suggests that $TiSi_2$ and B_4C preferentially react to form TiB_2, SiC, and Si at 1600 °C, as shown in Eq. (5):

$$TiSi_2 + 1/2B_4C = TiB_2 + 1/2SiC + 3/2Si \quad (5)$$

Furthermore, the Si product from Eq. (5) will not remain in the microstructure indefinitely but will continue to react with the matrix ZrC to form $ZrSi_2$ (Eq. (6)) and ZrSi (Eq. (7)):

$$ZrC + 3Si = ZrSi_2 + SiC \quad (6)$$

$$ZrC + 2Si = ZrSi + SiC \quad (7)$$

Subsequent XRD results confirmed that the reaction products

Table 1 Composition and sintering parameters for the ZrC-based ceramics

Sample	Composition of raw materials (mol%)				Sintering parameter
	$TiSi_2$: B_4C	ZrC	$TiSi_2$	B_4C	
ZTS-10B	2 : 1	85	10	5	1600 °C/40 MPa/3 min + 1800 °C/40 MPa/10 min
ZTS-20B		70	20	10	1600 °C/40 MPa/3 min + 1800 °C/40 MPa/10 min
ZTS-30B		55	30	15	1600 °C/40 MPa/3 min + 1800 °C/40 MPa/10 min
ZTS-30B-one step		55	30	15	1800 °C/40 MPa/13 min

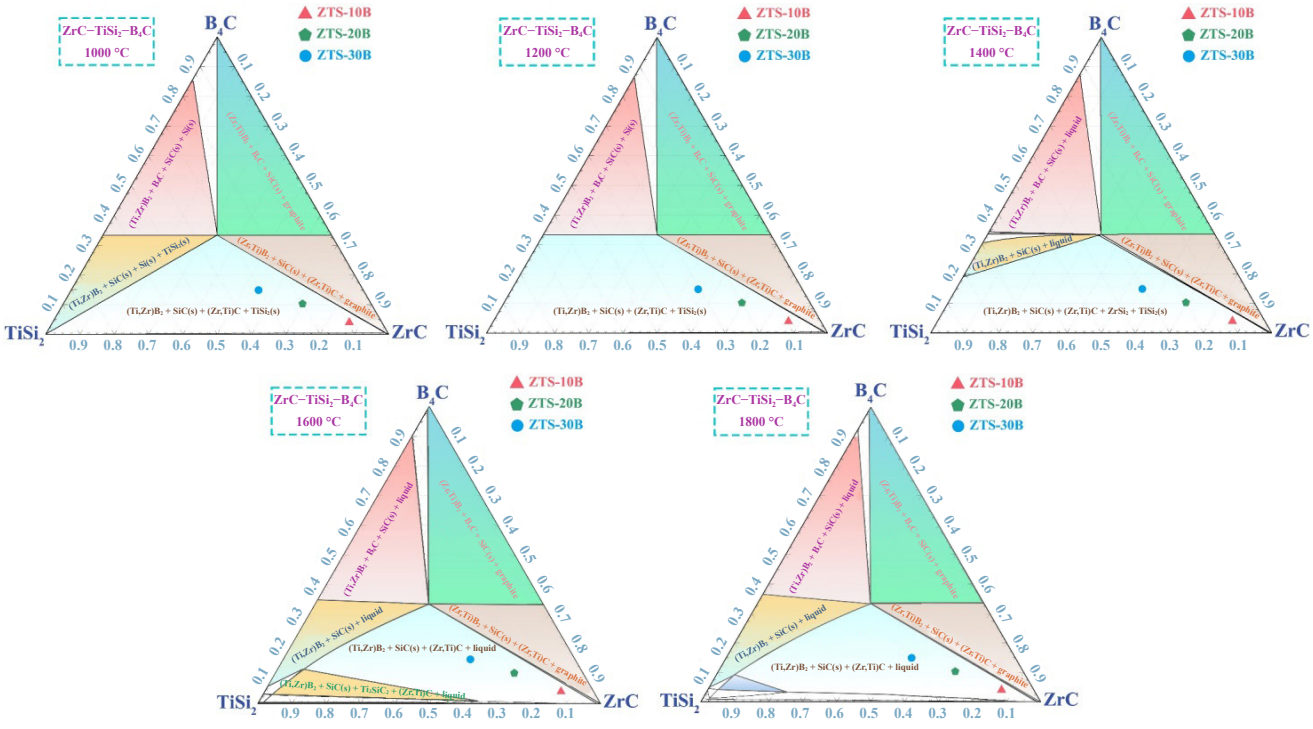

Fig. 1 Calculated phase diagrams of the ZrC–$TiSi_2$–B_4C system at 1000–1800 °C. Note: The apparent convergence of phase boundaries at a point is a graphical representation based on discrete equilibrium calculations; a minute multiphase region may exist at this composition.

between ZrC and Si primarily consist of $ZrSi_2$, which slightly differs from our previous findings on ZrC–Si reactions [22,33].

The thermodynamic evaluations were conducted using FactSage 7.1 software to calculate the phase content variations of each component with temperature, as shown in Figs. S1(b)–S1(d) in the ESM. The reaction between $TiSi_2$ and B_4C can proceed as early as 800 °C to form TiB_2 and SiC, with their contents remaining relatively stable with temperature changes.

3.2 Phase composition and solid solution formation

XRD analysis was performed on the sintered multiphase ceramics (Fig. 2(a)). When the $TiSi_2$ addition was 10 mol% (with 5 mol% B_4C), no diffraction peaks of $TiSi_2$ or B_4C were detected in the sintered ceramics; instead, diffraction peaks of the reaction products TiB_2 and β-SiC appeared, indicating a complete *in situ* reaction between them. However, no $ZrSi_2$ diffraction peak was observed in the ZTS-10B sample. When the Si content is low, C atoms from ZrC diffuse into Si, preferentially forming nonstoichiometric ZrC_{1-x} and SiC [22], as shown in Eq. (8):

$$ZrC + xSi = ZrC_{1-x} + xSiC \quad (8)$$

When the $TiSi_2$ addition increases to 20 mol%, the diffraction peaks of TiB_2 and SiC generated by the *in situ* reaction intensify, accompanied by the appearance of $ZrSi_2$ diffraction peaks, indicating that the reaction product Si begins to react with ZrC to form $ZrSi_2$.

For the three sintered multiphase ceramics, the diffraction peaks of ZrC and TiB_2 both exhibit significant shifts. As revealed by the magnified XRD patterns in Fig. 2(b), compared to the standard ZrC card (PDF#04-003-6212), the ZrC diffraction peaks in the sintered ceramics show varying degrees of high-angle shift. Additionally, the TiB_2 diffraction peaks show low-angle shifts relative to the standard TiB_2 card (PDF#01-071-5368), indicating Zr atoms with larger atomic radius dissolution into TiB_2. Therefore, the peak shifts of both ZrC and TiB_2 demonstrate that the $ZrSi_2$ liquid phase formed during sintering at 1600 and 1800 °C significantly promotes solid solution formation in carbides and diborides.

The refined lattice parameters and calculated weight fractions of each phase are presented in Table S1 in the ESM. The refined XRD patterns are shown in Figs. S2(a)–S2(c) in the ESM. For the (Zr,Ti)C solid solution, disregarding the effect of carbon vacancies on its lattice parameters, Vegard's law was employed to calculate the Ti solubility in (Zr,Ti)C (representing an upper estimate), as illustrated in Fig. 2(c). The *in situ* reaction between $TiSi_2$ and B_4C promotes mutual diffusion of Zr/Ti metal atoms, thereby enhancing their solubility in the solid solution.

In summary, the addition of $TiSi_2$ and B_4C enables the formation of a liquid phase at sintering temperatures (1600 and 1800 °C), which significantly promotes the solubility of Ti/Zr atoms in (Zr,Ti)C and $(Ti,Zr)B_2$ solid solutions. With increasing $TiSi_2$ content, the amounts of the three *in situ* reaction products—$(Ti,Zr)B_2$, SiC, and $ZrSi_2$—gradually increase. When the $TiSi_2$ addition reaches 30 mol%, abundant reinforcement/toughening phases are formed, thereby enhancing the mechanical properties of ZrC-based ceramics.

3.3 Densification behavior

Figure 3 presents the densification curves, densification rates, and relative densities of the multiphase ceramics. Each of the three compositions shows a marked rise in the densification rate at approximately 1300 °C, with distinct peaks occurring near the first holding temperature of 1600 °C. This behavior is ascribed to the *in situ* reaction between $TiSi_2$ and B_4C. At this stage, the interdiffusion process activated by the *in situ* reaction significantly improves mass transport, further enhancing densification.

The densification-rate peak observed near 1600 °C is primarily due to the *in situ* reaction of $TiSi_2$ and B_4C. When the temperature is raised to the second holding stage (1800 °C), another—although smaller—peak appears in the rate curve, suggesting that the *in situ* reaction is largely complete and that densification is now

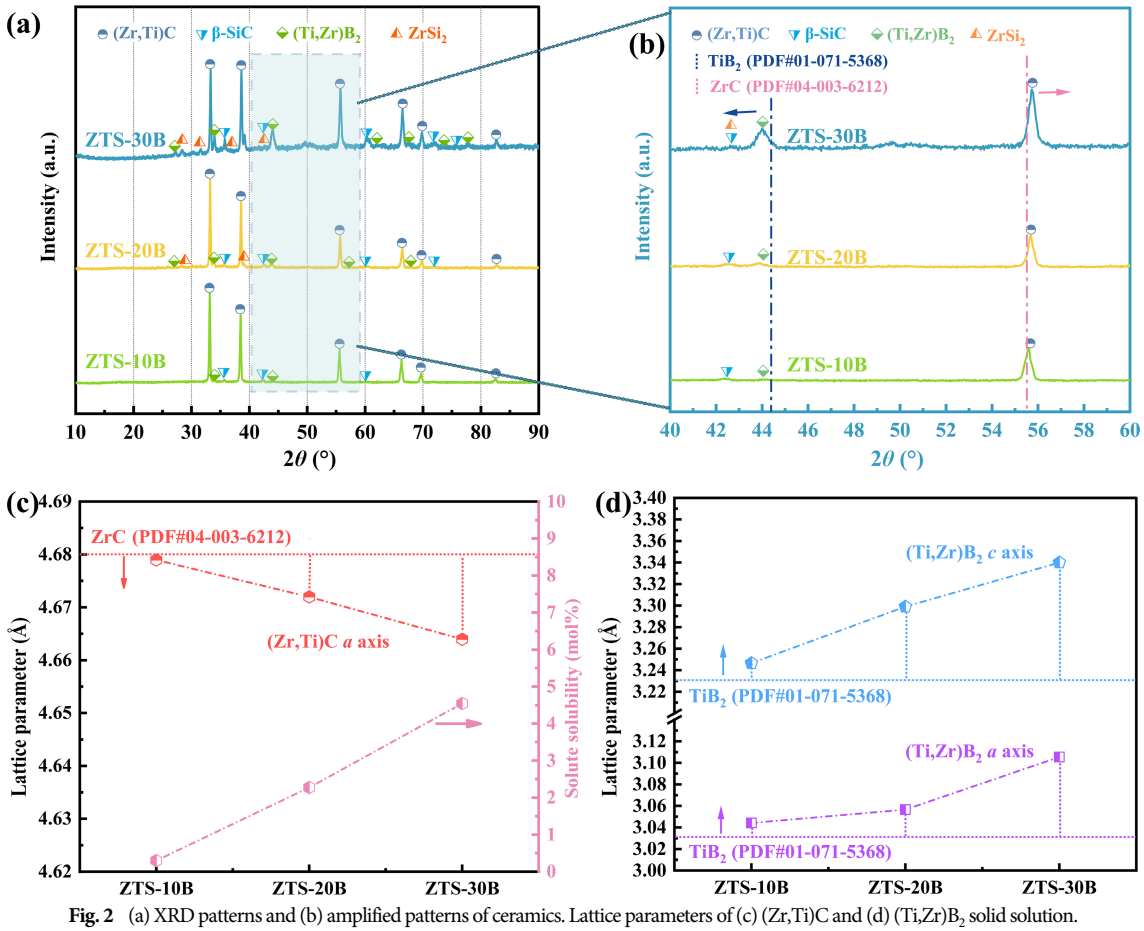

Fig. 2 (a) XRD patterns and (b) amplified patterns of ceramics. Lattice parameters of (c) (Zr,Ti)C and (d) $(Ti,Zr)B_2$ solid solution.

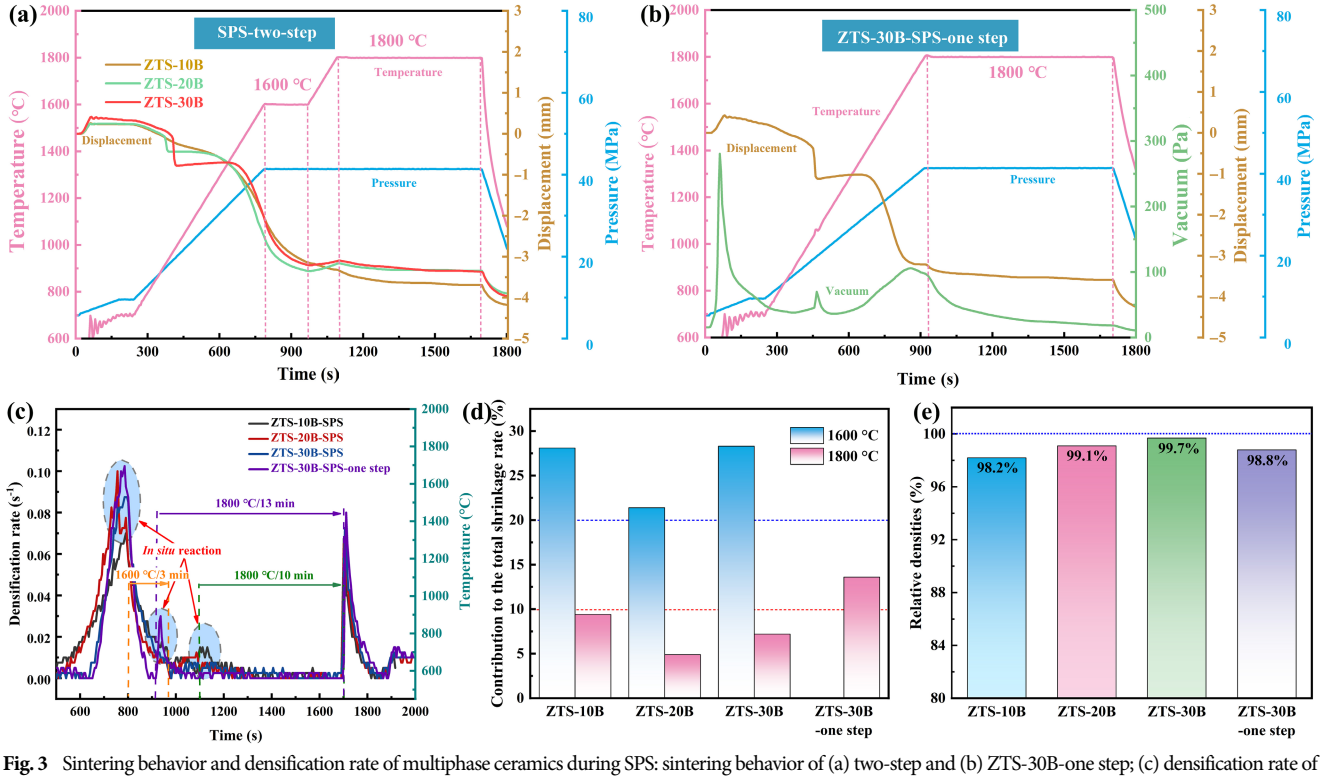

Fig. 3 Sintering behavior and densification rate of multiphase ceramics during SPS: sintering behavior of (a) two-step and (b) ZTS-30B-one step; (c) densification rate of multiphase ceramics; (d) contribution of shrinkage at each stage to total shrinkage; (e) RD of multiphase ceramics.

dominated by atomic inter-diffusion. This stage involves two main mechanisms: (1) Because 1800 °C exceeds the melting points of the reaction products Si and $ZrSi_2$, both transform into a liquid phase. The resulting liquid significantly enhances atomic mobility.

(2) At this temperature, Zr/Ti and C/B atoms continue to interdiffuse, leading to the formation of carbide/boride solid solutions. Owing to the relatively low diffusion coefficients of the metal atoms (Zr,Ti) compared with the non-metal species (C,B) [34], solid-solution formation lags behind the reaction step. Thus, metal-atom diffusion occurs mainly during the second sintering stage at 1800 °C. During the first-step reaction (1600 °C), the gradual increase in free metal atom concentration provides sufficient thermodynamic conditions for the second-step solid solution process. Additionally, the higher holding temperature (1800 °C) and prolonged holding time (10 min) compared to the first step offer kinetic assurance for Ti/Zr diffusion and solid solution.

The densification rate curve for the one-step process shows a prominent peak at the onset of the 1800 °C hold, indicating that intense *in situ* reactions still occur at this stage. Excessively high reaction temperatures tend to accelerate Ostwald ripening in the matrix, ultimately leading to grain coarsening, which in turn inhibits densification [35]. In contrast, the curve for the two-step process shows a much lower rate peak at 1800 °C, confirming that the major reactions are largely complete after the first step.

The contributions to the total shrinkage from the 1600 °C reaction stage and the 1800 °C diffusion stage for both the two-step and one-step processes were calculated, as shown in Fig. 3(d). For all three compositions fabricated via the two-step schedule, the shrinkage during the 1600 °C holding stage exceeds 20% of the total shrinkage. This substantial contribution quantitatively confirms that the *in situ* reactions and the associated liquid phase formation are the primary drivers for the initial, rapid densification. This low-temperature, reaction-driven consolidation effectively suppresses grain growth of the ZrC matrix. In contrast, the shrinkage during the 1800 °C hold is less than 10% of the total. This minor contribution aligns with the low densification rate peak observed in Fig. 3(c) and confirms that the major reactions are largely complete. Densification at this stage is primarily governed by diffusion-controlled processes, such as final pore removal and grain boundary adjustment. For the one-step sintered sample (same final temperature and total time), the shrinkage occurring specifically during the 1800 °C hold is significantly higher than in the two-step process. This directly demonstrates that intense *in situ* reactions are still ongoing at the peak temperature in the one-step schedule. As previously discussed, such high-temperature reactions accelerate Ostwald ripening in the matrix, ultimately leading to grain coarsening and a less refined final microstructure. Figure 3(e) shows that ceramics prepared via the one-step method exhibit lower density than those fabricated by the two-step method.

In summary, the 1600 °C step is reaction-driven for rapid consolidation, while the 1800 °C step is diffusion-driven for microstructural perfection and solid solution formation. The densification in multiphase ceramics evolves from a reaction-driven interdiffusion stage to a stage governed by lattice diffusion of metal atoms (Ti,Zr). Initially, kinetics are controlled by the reaction-diffusion between $TiSi_2$ and B_4C, with concomitant liquid phase formation promoting particle rearrangement. Subsequently, the mechanism shifts to metal-atom-dominated lattice diffusion, where the mobility of Ti and Zr becomes rate-limiting. Concurrently, the liquid-phase sintering induced by the reaction product $ZrSi_2$ exerts a synergistic effect, further promoting densification. The addition of $TiSi_2$ and B_4C phases enhances atomic transport capability, promotes mutual diffusion and solid solution of atoms, and achieves phase reconstruction, collectively advancing the densification process.

3.4 Microstructure

Figure 4 shows the backscattered electron (BSE) images of the multiphase ceramics prepared by two-step SPS. For ZTS-10B, the microstructure primarily consists of three phases: a white matrix phase, plate-like gray phases, and nanoscale black dispersed phases. With increasing $TiSi_2$ and B_4C addition, dark-white grains appear within the white matrix phase, while the amounts of plate-like gray phases and nanoscale black dispersed phases increase proportionally. Energy dispersive spectroscopy (EDS) analysis was performed on the microstructure of the multiphase ceramics (Fig. S3 in the ESM). The results reveal that the white matrix phase corresponds to (Zr,Ti)C, the plate-like gray phase to $(Ti,Zr)B_2$, the black nanoscale dispersed phase to SiC, and the few dark-white granular particles to $ZrSi_2$. Figure S4 in the ESM statistically presents the average grain sizes of each phase in the sintered ceramics. With increasing $TiSi_2$ and B_4C addition, the grain sizes of all phases significantly decrease. Particularly in ZTS-30B, all phases exhibit fine and dispersed distributions, with grain sizes below 1 μm, reaching the nanoscale.

To further investigate its microstructure, STEM analysis was performed on ZTS-30B, as shown in Fig. 5. The HAADF-STEM image in Fig. 5(a) reveals the presence of four distinct phases: a light-gray solid solution phase (I), finely dispersed dark nanoparticles (II), light-black plate-like grains (III), and dark-gray irregular grains (IV) with moderate atomic contrast relative to the matrix. Based on elemental mapping and EDS analysis, the light-gray phase (I) was identified as (Zr,Ti)C. The finely dispersed dark nanoparticles (II) correspond to SiC, while the light-black plate-like grains (III) were confirmed as $(Ti,Zr)B_2$ solid solution. For the dark-gray irregular grains (IV), EDS results showed significant Zr content along with a considerable amount of Si but nearly no B or C, suggesting that the phase is $ZrSi_2$. Notably, approximately 6 at% Ti was detected in these grains, indicating the formation of a $(Zr,Ti)Si_2$ solution.

Our recent studies on the strengthening and toughening mechanisms of ZrC/TiC ceramics have demonstrated that plate-like TiB_2 significantly enhances the toughness of carbide ceramics [36–40], while dispersed nanosized SiC particles contribute to strength improvement via physical pinning [22,33,41–44]. Therefore, a detailed examination was conducted on the *in situ* formed TiB_2, SiC, and $ZrSi_2$ in the ZTS-30B sample (Fig. 5(b)). The toughening phase, plate-like TiB_2, exhibits a refined morphology with lengths below 500 nm. In contrast, the strengthening phase, SiC, displays two distinct distribution patterns. One type of SiC is located adjacent to the TiB_2 grains, exhibiting an "accompanying" morphology. This SiC primarily originates from the *in situ* reaction between $TiSi_2$ and B_4C at 1600 °C (Eq. (5)) and can be referred to as primary SiC. The other type of SiC is distributed along the ZrC grain boundaries, showing a clear grain-boundary pinning effect. This variant of SiC results from the reaction between Si and the ZrC matrix (Eq. (6)).

Figure 6(a) shows a bright-field (BF) image of the *in situ* products and matrix in the ZTS-30B sample, further confirming the nanoscale grain characteristics of all phases. The EDS results in Fig. 6(b) reveal that the solid solubility of Zr in $(Ti,Zr)B_2$ reaches 10.3 at%, whereas the solubility of Ti in (Zr,Ti)C is 7.5 at%, based on the Ti/Zr atomic ratios. The selected area electron diffraction (SAED) patterns (Fig. 6(c)) confirm that the matrix consists of face-centered cubic (FCC) (Zr,Ti)C solid solution, the plate-like grains are hexagonal $(Ti,Zr)B_2$, and the SiC particles correspond to twinned β-SiC with an FCC structure. The twinned structure is a common growth feature of β-SiC crystallized under the present

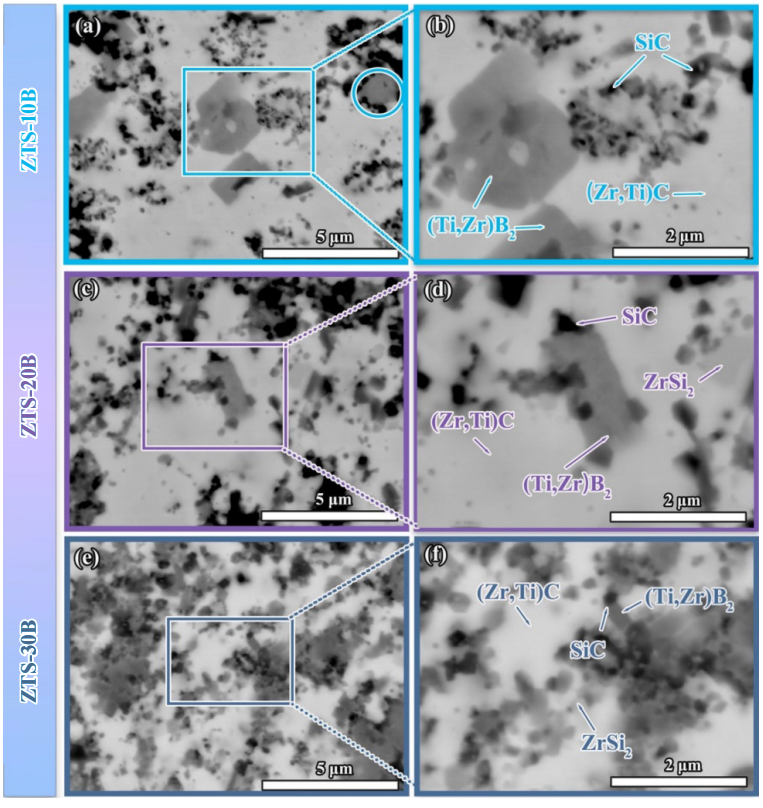

Fig. 4 BSE images of sintered ceramics: (a, b) ZTS-10B; (c, d) ZTS-20B; (e, f) ZTS-30B.

sintering conditions, which is mainly attributed to the high density of SFs within the grains.

Figure 6(d) displays high-resolution TEM (HRTEM) images of the interfaces between $(Ti,Zr)B_2$ grains and adjacent $(Ti,Zr)B_2$, (Zr,Ti)C, and β-SiC phases. No specific crystallographic orientation relationship was observed between adjacent $(Ti,Zr)B_2$ grains. HRTEM analysis revealed no distinct orientation relationships at the interfaces between $(Ti,Zr)B_2$ and either (Zr,Ti)C or β-SiC. Notably, at the $(Ti,Zr)B_2$/β-SiC interface, subgrains of β-SiC with sizes of approximately 10 nm were observed. These nanograins originate from the *in situ* reaction between $TiSi_2$ and B_4C (Eq. (5)) and can be identified as primary SiC. A coherent interface was evident between these nanocrystals and the surrounding β-SiC grains. The presence of such nanoscale SiC grains further demonstrates that the recrystallization process during the *in situ* reaction effectively promotes microstructural refinement.

Figure 6(e) presents the interfacial relationship between the (Zr,Ti)C matrix and the *in situ* formed β-SiC. Initial observation along the β-SiC $[0\bar{1}1]$ zone axis revealed a specific crystallographic orientation relationship between SiC and the matrix through Fourier transform analysis: (111)SiC//(200)(Zr,Ti)C, $[0\bar{1}1]$SiC// [013](Zr,Ti)C. This orientation relationship suggests that the FCC SiC formed via the *in situ* reaction between ZrC and Si (Eq. (8)) and maintained a specific orientation with the original FCC matrix. Such crystallographic coherence reduces lattice mismatch at the interface, effectively impedes dislocation motion to enhance deformation resistance [45], and improves stress transfer to delay premature failure, thereby increasing toughness [46]. Furthermore, a high density of SFs was observed in β-SiC, which are generally categorized into growth faults (or twin faults) and deformation faults [47]. In this study, the SFs are identified as growth faults, commonly associated with the glide of partial dislocations [48]. These SFs were observed on the $(1\bar{1}\bar{1})$ planes. As planar defects, the high density of SFs effectively hinders dislocation motion and enhances the ceramic's resistance to deformation.

Subsequently, the interface was examined along the $[\bar{1}11]$ zone axis of (Zr,Ti)C. In this orientation, no distinct crystallographic relationship was detected between SiC and (Zr,Ti)C. However, Fourier transform analysis of the (Zr,Ti)C matrix revealed two distinct diffraction patterns. Most regions exhibited diffraction spots corresponding to the disordered FCC ZrC, while areas adjacent to SiC showed additional weak-intensity spots at the midpoints between the primary ZrC reflections. Based on our previous studies on ZrC_{1-x} ceramics, these weaker spots are attributed to an ordered vacancy phase, Zr_2C [49]. In the present case, localized Si enrichment near ZrC grains promotes extensive outward diffusion of carbon atoms, significantly increasing the carbon vacancy concentration and facilitating the formation of the ordered Zr_2C phase, as represented by Eq. (9):

$$2ZrC + Si = Zr_2C + SiC \tag{9}$$

The formation of $(Ti,Zr)B_2$ and (Zr,Ti)C solid solutions primarily originates from the interdiffusion of metal atoms (Ti and Zr) between TiB_2 and ZrC. The EDS mapping results in Fig. 7(a) clearly show Zr enrichment within the plate-like TiB_2 grains, while a detectable amount of Ti is also present in the ZrC matrix. Figure 7(b) displays the compositional profiles across the (Zr,Ti)C/$(Ti,Zr)B_2$ interface obtained by EDS line scan. A distinct interdiffusion zone of approximately 9 nm is observed at the interface.

It is noteworthy that the bright-field-transmission electron microscopy (BF-TEM) image in Fig. 7(c) reveals the presence of elliptical nanoprecipitate (I) and lath-shaped nanoprecipitate (II) within the SiC grains, both with sizes of approximately 40 nm. EDS analysis indicates that the elliptical nanoprecipitate is rich in Si and Zr, along with a considerable amount of C, which may

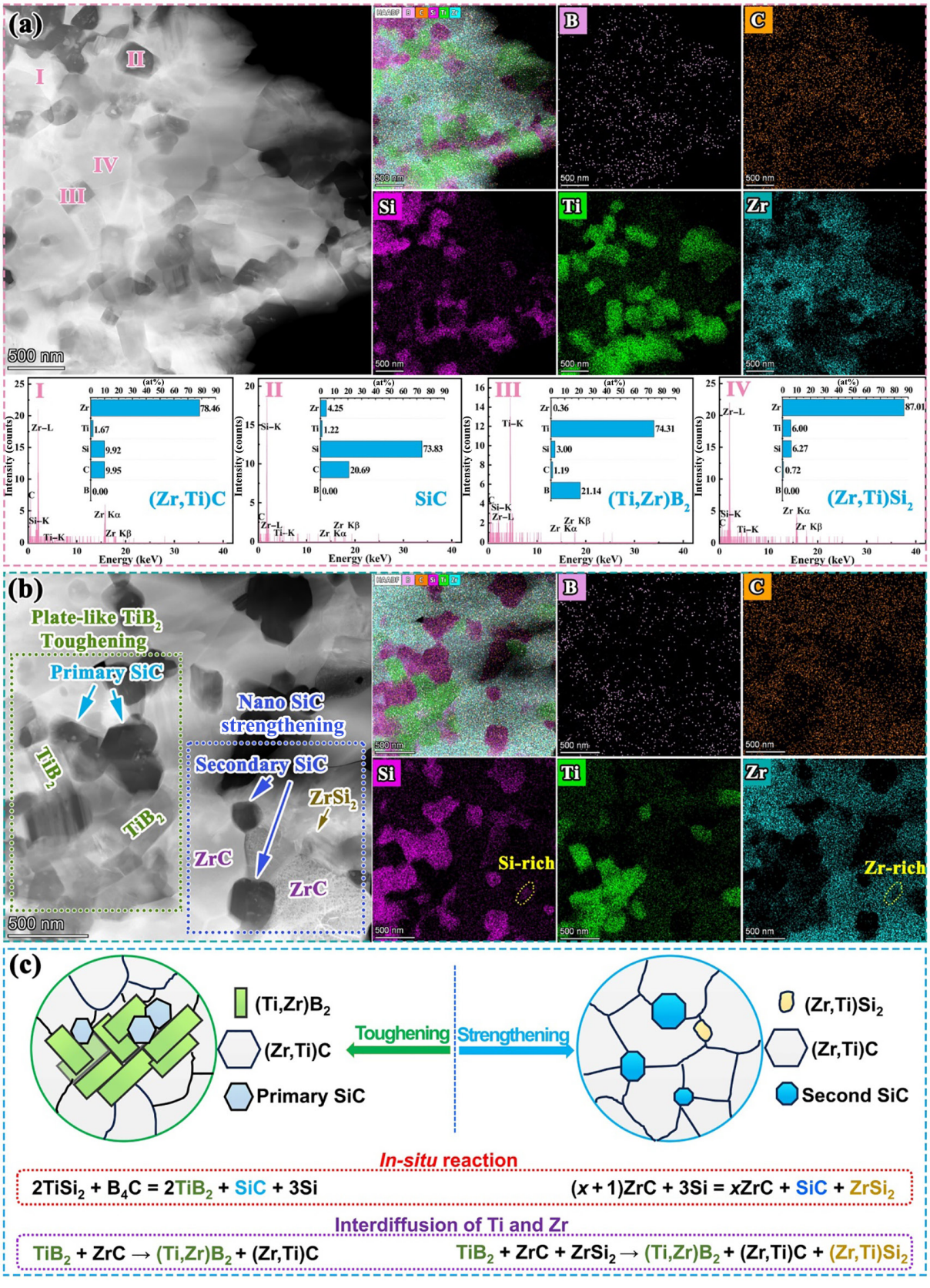

Fig. 5 (a) STEM-HAADF image and EDS spectra of ZTS-30B sample; (b) EDS elemental mapping results of strengthening and toughening phases in ZTS-30B sample; (c) schematic diagram elucidating their formation mechanism.

originate mainly from the surrounding SiC grains. Closer examination of the BF image shows that this elliptical particle is not located inside the SiC grain but rather resides at the grain boundaries between two SiC particles. Their irregular elliptical morphology is characteristic of grains formed from liquid phase solidification. Combined with the elemental analysis, these

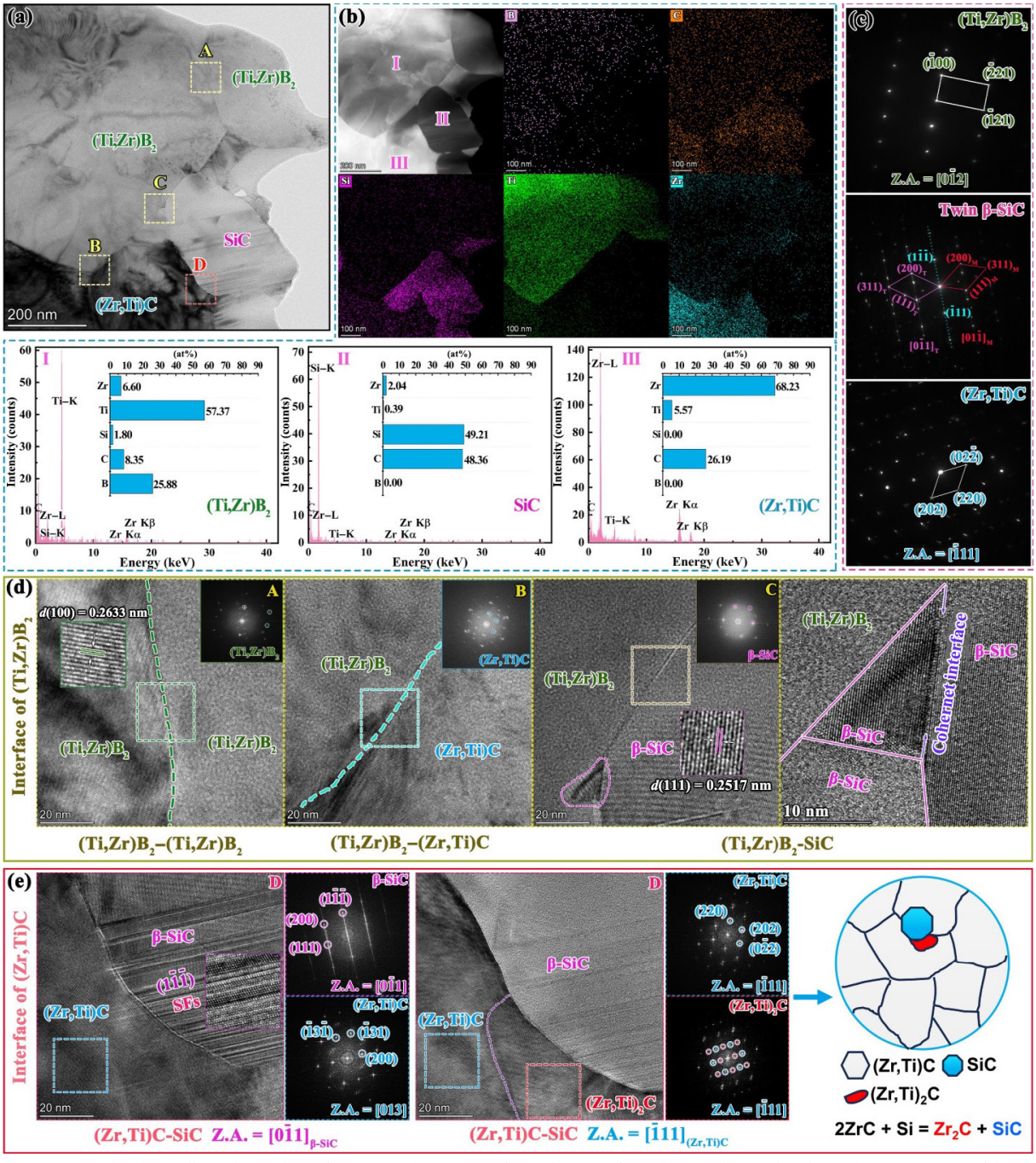

Fig. 6 Microstructural and crystallographic analysis of ZTS-30B: (a) BF image of interphase interfaces; (b) EDS elemental analysis; (c) SAED patterns of the identified phases; (d) HRTEM images of interfaces between $(Ti,Zr)B_2$ and adjacent phases; (e) HRTEM images of (Zr,Ti)C/SiC interface.

elliptical nanocrystals are identified as $ZrSi_2$, incorporating a small amount of Ti in solid solution. According to Eq. (6), $ZrSi_2$ is expected to be situated adjacent to the (Zr,Ti)C and SiC grains. However, the formation of a liquid phase during sintering provided high atomic mobility, enabling the deviation of this $ZrSi_2$ grain from the (Zr,Ti)C grain boundaries. In contrast, the lath-shaped nanoprecipitate (II) found within the SiC grain is rich in Ti, Si, and C. Its morphology is similar to the typical layered structure of Ti_3SiC_2, suggesting that it is likely a Ti_3SiC_2 phase.

Therefore, based on a two-step SPS approach, this work proposes a structural design concept for the *in situ* construction of multiscale architectural ZrC-based ceramics. This strategy integrates atomic-scale solid solution strengthening, nanoscale SiC pinning reinforcement, and submicron-scale TiB_2-SiC toughening mechanisms, aiming to achieve comprehensive performance improvement through synergistic effects across different scales. First, the atomic-scale strengthening effect of solid solutions: Through *in situ* reactions and liquid-phase sintering, Zr/Ti-mutually dissolved $(Ti,Zr)B_2$ and (Zr,Ti)C solid solutions are formed. The heterogeneous atoms within the solid solutions introduce strain fields into the crystal lattice, thereby impeding dislocation motion and enhancing the resistance to plastic deformation of ceramics. Second, nanoscale pinning reinforcement by SiC: Both the primary and secondary SiC phases formed during sintering contribute significantly to the strength of ceramics. The presence of these nanosized particles enhances strength via the "particle strengthening" mechanism while also improving toughness and wear resistance. Third, the submicron-

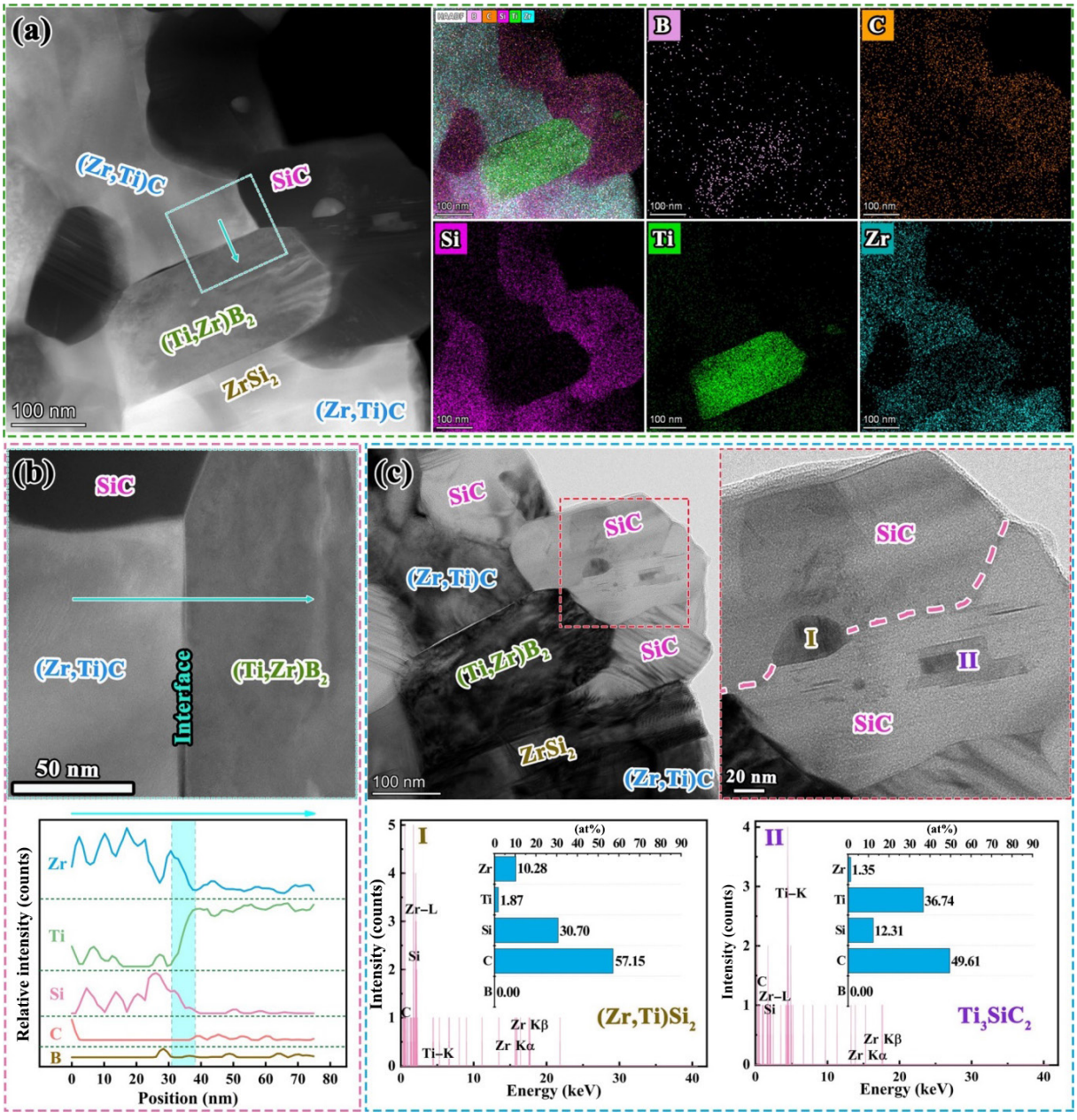

Fig. 7 (a) HAADF image and EDS mappings of (Zr,Ti)C/(Ti,Zr)B_2 interface in ZTS-30B sample; (b) EDS line scan across interface; (c) BF-TEM image and point EDS of intragranular nanoprecipitates in SiC.

scale toughening mechanism of plate-like TiB_2: The plate-like TiB_2 grains promote toughening by deflecting propagating cracks along tortuous intergranular paths, thereby increasing the crack propagation length and energy dissipation. Simultaneously, these plate-like grains can form physical bridges across crack surfaces, distributing stress through interfacial friction and localized plastic deformation.

3.5 Mechanical properties

Table S2 in the ESM summarizes the mechanical properties of the ZrC-based multiphase ceramics prepared via the two-step reactive SPS in this study, alongside relevant data from Refs. [9–12,15,17,20–22,50–57] for comparison. The observed lower sintering temperature and higher RD can be attributed to liquid-phase sintering facilitated by $TiSi_2$/Si and the *in situ* reactions. In this work, the H_v of ZTS-10B (with 10 mol% $TiSi_2$ and 5 mol% B_4C) is approximately 18.0 GPa, showing a slight improvement over monolithic ZrC [10,11,22]. This increase is primarily due to the formation of harder phases, namely, TiB_2 (~28.5 GPa [58]) and SiC (26.5–32.8 GPa [59]). However, the limited content of TiB_2 (2.7 wt%) and SiC (3.6 wt%) in ZTS-10B results in only a modest hardness enhancement. As the $TiSi_2$ addition increases to 20 mol%, the *in situ* reaction concurrently yields 6.5 wt% $ZrSi_2$. Given that $ZrSi_2$ has a significantly lower H_v of only 10.547 GPa [60], the overall hardness of the composite decreases to 16.2 GPa. With a further increase in $TiSi_2$ to 30 mol%, although the $ZrSi_2$ content also rises, the contents of the hardening phases TiB_2 and SiC increase concurrently. Moreover, the liquid phase promotes the formation of (Ti,Zr)B_2 and (Zr,Ti)C solid solutions, contributing to solid solution hardening. Consequently, the hardness of the ZTS-30B composite recovers to 18.1 GPa. The measured E for the optimal ZTS-20B composition is approximately 412±7 GPa. While this value is comparable to or slightly higher than that of monolithic ZrC (395±15 GPa [10]), the improvement is not as

pronounced as the enhancements in strength and toughness. This result is consistent with the multiphase nature of the composite. The *in situ* formed high-modulus phases, TiB_2 (~594 GPa [61]) and SiC (~470 GPa [62]), contribute to increasing the overall stiffness. However, the simultaneous formation of the $ZrSi_2$ phase, which has a significantly lower modulus (~212 GPa [63]), offsets part of this reinforcing effect. Overall, while the addition of $TiSi_2$ and B_4C leads to some fluctuation in the hardness and E of the ZrC-based ceramics, it results in a significant improvement in both flexural strength and K_{IC}.

The flexural strength of the multiphase ceramics fabricated in this study increases significantly with higher $TiSi_2$ additions, rising from 745 MPa for ZTS-10B to 824 MPa for ZTS-30B. This outstanding flexural strength of the ZrC–$TiSi_2$–B_4C system considerably surpasses that of most previously reported ZrC-based ceramics. It exceeds the 513–585 MPa reported for ZrC–TiB_2 systems [17] and the 626 MPa for ZrC–SiC systems [21]. The exceptional flexural strength is attributed to the unique microstructure of the multiphase ceramics: (1) Ultrafine submicron microstructure enabled by low-temperature *in situ* reactions. The *in situ* reactive SPS process achieves full densification, effectively suppressing abnormal grain growth and resulting in an average matrix grain size below 500 nm (ZTS-30B). (2) Atomic-scale: solid solution strengthening via multiphase solid solutions. The liquid-phase reaction products (Si/$ZrSi_2$) promote diffusion, leading to the formation of (Ti,Zr)B_2 and (Zr,Ti)C solid solutions, which provide substantial solid solution strengthening. (3) Nanoscale: pinning reinforcement by nanosized SiC particles. Primary SiC particles, mainly pinning the associated (Ti,Zr)B_2 grains, inhibit the growth of (Ti,Zr)B_2. Secondary SiC particles, primarily located at the (Zr,Ti)C matrix grain boundaries with a specific orientation relationship to the matrix (Fig. 6(e)), impede dislocation glide and alleviate stress concentration, thereby enhancing flexural strength. (4) Microscale: Formation of a significant fraction of the fine TiB_2 reinforcing phase: The reinforcing (Ti,Zr)B_2 phase exhibits good chemical compatibility and interfacial bonding with the (Zr,Ti)C matrix, further enhanced by a Ti/Zr interdiffusion layer (Fig. 7(b)).

In this study, the K_{IC} of ZTS-10B shows only a moderate increase to 4.8 MPa·$m^{1/2}$ compared to other ZrC-based ceramics, which is mainly attributed to the limited formation of TiB_2 and SiC at this composition. However, when the $TiSi_2$ addition increases to 20 mol%, the K_{IC} of the composite rises significantly to 6.4 MPa·$m^{1/2}$. This improvement stems from two contributing factors. First, compared to ZTS-10B, the *in situ* reaction products at this composition include a noticeable amount of $ZrSi_2$. Given that $ZrSi_2$ possesses a higher intrinsic K_{IC} (6.905 MPa·$m^{1/2}$ [60]) than the ZrC matrix, its presence can dissipate more energy during fracture, thereby enhancing the overall toughness of the composite. Second, the yield of *in situ* formed TiB_2 and SiC is also substantially greater than that in ZTS-10B, further contributing to the toughness increase. The ZTS-30B composite achieves a K_{IC} as high as 7.5 MPa·$m^{1/2}$. In this sample, the contents of all three toughening phases—TiB_2, SiC, and $ZrSi_2$—reach their highest levels among the studied compositions, synergistically promoting superior K_{IC}.

To elucidate the fracture modes and toughening mechanisms of the multiphase ceramics, their fracture surfaces and crack propagation paths were examined. Figures 8(a)–8(f) present BSE and secondary electron (SE) images of the fracture morphologies for the three composites. When the $TiSi_2$ addition is raised to 30 mol%, the composite displays the finest average grain size and shows the formation of distinct SiC–(Ti,Zr)B_2 aggregate structures acting as toughening phases. Intergranular fracture and pronounced surface roughness are most evident in this sample. Moreover, the fracture morphology of these aggregates resembles that reported for SiC–TiB_2 composites [64], further confirming that the SiC–(Ti,Zr)B_2 aggregates serve as effective toughening constituents.

To gain further insight into the toughening mechanisms, Figs. 8(g)–8(i) present BSE images and corresponding schematics illustrating crack propagation in the ZTS-30B composite. It is evident that cracks propagate preferentially along the interfaces between the (Zr,Ti)C matrix and the (Ti,Zr)B_2 particles, which aligns well with the intergranular fracture features of (Ti,Zr)B_2 observed in Figs. 8(a)–8(f). Neglecting the impact of solid solution, the coefficients of thermal expansion (CTE) of (Zr,Ti)C and (Ti,Zr)B_2 can be approximated by the values for ZrC (6.7×10^{-6} K^{-1} [65]) and TiB_2 (7.9×10^{-6} K^{-1} [66]), respectively. The mismatch in CTE between these phases generates significant residual stress at the (Zr,Ti)C–(Ti,Zr)B_2 interface. This promotes crack deflection and prolongs the crack propagation path, thereby contributing to toughness enhancement. Furthermore, the nonuniform distribution of residual stress can induce microcracking at the tips of propagating cracks, leading to crack branching. The CTE of (Zr,Ti)C is higher than that of SiC (4.35×10^{-6} K^{-1} [67]), causing cracks to extend through SiC particles rather than along their interfaces. Since SiC possesses a higher inherent toughness than ZrC, this transgranular fracture process consumes additional energy, improving the overall K_{IC} of the ZrC matrix. More importantly, considering the significant CTE difference between SiC and TiB_2, cracks within SiC–TiB_2 aggregates undergo pronounced deflection along the SiC/TiB_2 interfaces. This extends and tortuously redirects the crack path, dissipating substantial energy—a toughening effect analogous to that reported for SiC–TiB_2 aggregates in B_4C-based systems [24, 25]. Additionally, a crack-bridging mechanism associated with weakened interfaces is observed within SiC grains [68]. Crack bridging primarily initiates at crack tips inside SiC grains. When a crack propagates into a SiC grain, the grain can form bridging ligaments that partially counteract the applied stress at the crack tip. This stress redistribution hinders crack advance and may induce new crack nucleation nearby, ultimately forming a bridging configuration [69]. In summary, the synergistic operation of the aforementioned fracture modes collectively enhances the toughness of the fabricated composites.

Among all toughening mechanisms, SiC–TiB_2 agglomerates are proposed as the primary toughening source due to their substantial fraction and highly effective, geometry-based crack deflection/bridging mechanism. The $ZrSi_2$ phase provides essential intrinsic energy absorption, and Ti_3SiC_2 may offer nanoscale plasticity. The superior toughness of ZTS-30B arises from this hierarchical, multimechanism strategy where the agglomerates govern the main crack path, and the other phases augment energy dissipation at different scales.

In addition, we compared the flexural strength and K_{IC} of the multiphase ceramics prepared in this study with literature data, as shown in Fig. 9. Notably, compared to reported ZrC-based multiphase ceramics, the ZTS-30B composite in this work exhibits superior overall mechanical properties, with a flexural strength of 824±46 MPa and a K_{IC} of 7.5±0.5 MPa·$m^{1/2}$, significantly exceeding those of most ZrC-based materials. This performance advantage primarily originates from two mechanisms. On the one hand, $TiSi_2$ acts as a reactive sintering aid, effectively promoting densification through transient liquid-phase sintering. This enables the fabrication of nearly fully dense ZrC-based multiphase ceramics at relatively low temperatures. Concurrently, the *in situ* formed nanosized SiC particles exert a pinning effect within both

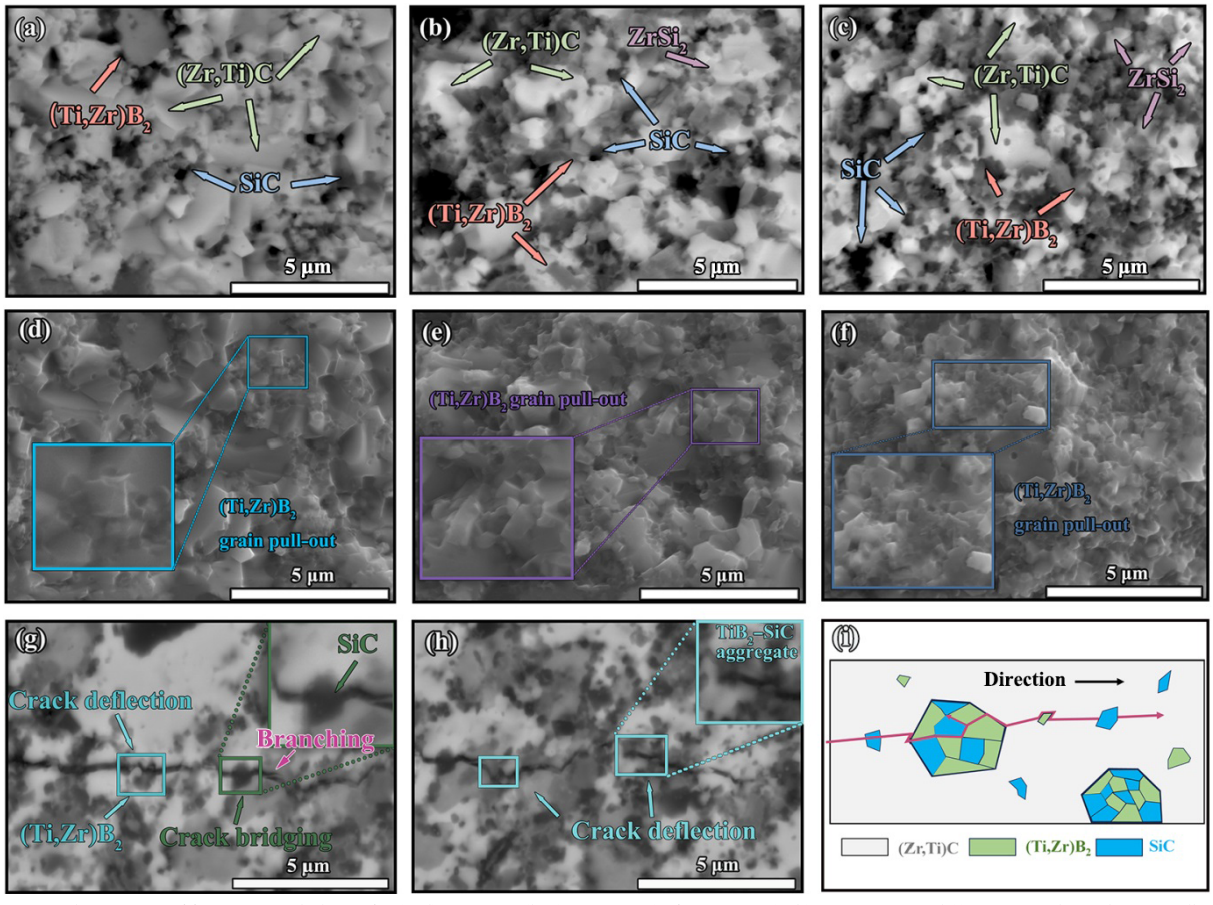

Fig. 8 BSE and SE images of fracture morphologies for (a, d) ZTS-10B; (b, e) ZTS-20B; (c, f) ZTS-30B. (g, h) BSE images and (i) corresponding schematics illustrating crack propagation in ZTS-30B sample.

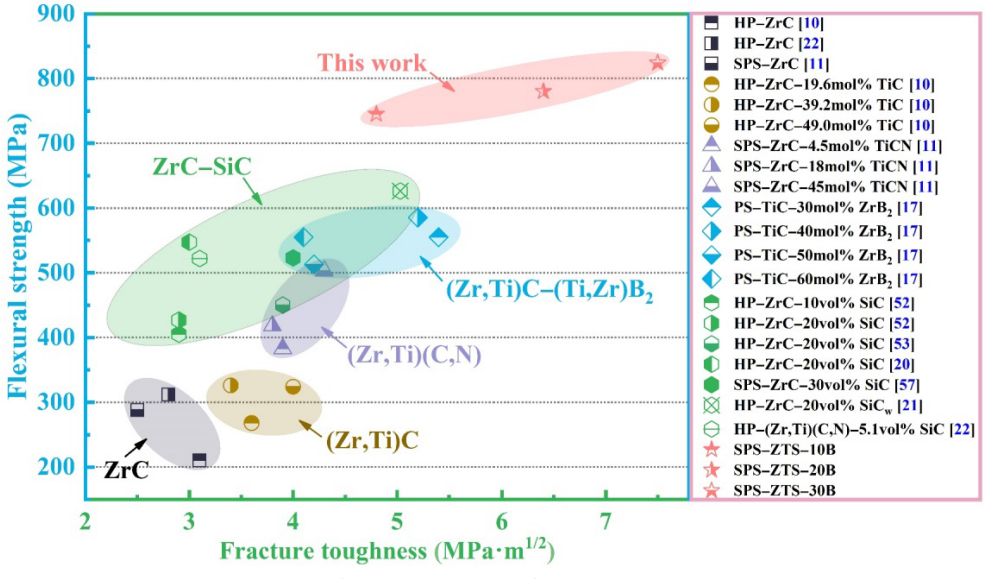

Fig. 9 Comparative study on flexural strength and K_{IC} from this work and other ZrC-based ceramics.

TiB_2 and ZrC grains, contributing to a uniform and refined microstructure, which positively influences the final properties. Furthermore, the liquid-phase *in situ* reaction products ($Si/ZrSi_2$) enhance atomic diffusion, leading to the formation of $(Ti,Zr)B_2$ and (Zr,Ti)C solid solutions, thereby providing substantial solid solution strengthening. On the other hand, the SiC–TiB_2 aggregates introduced into the ZrC matrix serve as a composite toughening phase. The interlocked structure of SiC and TiB_2 within these aggregates effectively deflects propagating cracks and extends the crack path [70], further enhancing the K_{IC}. Additionally, $ZrSi_2$, which possesses high intrinsic K_{IC}, dissipates considerable energy during fracture, synergistically improving the overall toughness of the composite.

In summary, based on a multiscale microstructure design and utilizing a two-step *in situ* reactive SPS process, this study successfully constructed ZrC-based ceramics with high strength

and toughness. This was achieved by integrating solid solution strengthening (atomic scale), nano-SiC pinning reinforcement (nanoscale), and SiC–TiB_2 aggregate toughening (microscale), resulting in the simultaneous enhancement of both strength and toughness in ZrC-based multiphase ceramics. This work provides critical insights into the microstructure design and mechanical property optimization of ultrahigh-temperature carbide ceramics.

4 Conclusions

A multiscale microstructure design was implemented to fabricate ZrC-based ceramics via a two-step *in situ* reactive SPS process using ZrC, $TiSi_2$, and B_4C powders as raw materials. With increasing $TiSi_2$ addition, the content of the three *in situ* reaction products—(Ti,Zr)B_2, SiC, and $ZrSi_2$—progressively increased. $TiSi_2$ preferentially reacts with B_4C to form TiB_2 and primary SiC, where the primary SiC particles pin the TiB_2 grain boundaries and inhibit their growth. Subsequently, the *in situ* generated Si reacts with the ZrC matrix to produce $ZrSi_2$ and secondary SiC. Acting similarly to grain-boundary pinners, the secondary SiC particles contribute to the formation of a submicron-scale structure with an average grain size below 500 nm. The ZTS-30B ceramics (ZrC with 30 mol% $TiSi_2$ and 15 mol% B_4C) exhibits superior mechanical properties, with a flexural strength of 824±46 MPa and a K_{IC} of 7.5±0.5 MPa·$m^{1/2}$, outperforming most reported ZrC-based materials. This performance enhancement is attributed to the following factors: $TiSi_2$ acts as a reactive sintering aid that promotes densification via transient liquid-phase formation; the pinning effect of *in situ* formed SiC refines the microstructure; and the synergistic toughening effect arises from both the SiC–TiB_2 composite aggregates and the high-toughness $ZrSi_2$ phase. This study successfully achieves a simultaneous improvement in both the strength and toughness of ZrC-based ceramics, providing important insights for the development of high-performance ultrahigh-temperature carbide ceramics.

Acknowledgements

This work was financially supported by the National Natural Science Foundation of China (Nos. 52002098 and 52002003) and the Heilongjiang Provincial Natural Science Foundation of China (No. LH2023E080). The support of thermodynamic calculations with FactSage® software given by Professor Yudong Fu (College of Material Science and Chemical Engineering, Harbin Engineering University) is also acknowledged.

Availability of data and materials

The data that support the findings of this study are available from the corresponding author upon reasonable request.

Competing interests

The authors have no competing interests to declare that are relevant to the content of this article.

Electronic Supplementary Material

Supplementary material is available in the online version of this article at https://doi.org/10.26599/JAC.2026.9221263.

References

[1] Cui KK, Mao HB, Zhang YY, *et al.* Microstructure, mechanical properties, and reinforcement mechanism of carbide toughened ZrC-based ultra-high temperature ceramics: A review. *Compos Interface* 2022, **29**: 729–748.

[2] Fahrenholtz WG, Hilmas GE. Ultra-high temperature ceramics: Materials for extreme environments. *Scripta Mater* 2017, **129**: 94–99.

[3] Gaffin N, Ade B, Crotzer T, *et al.* Design and fabrication of TRISO based ZrC fuel for nuclear thermal propulsion. *J Nucl Mater* 2025, **605**: 155538.

[4] Xin XT, Bao WC, Wang XG, *et al.* Reduced He ion irradiation damage in ZrC-based high-entropy ceramics. *J Adv Ceram* 2023, **12**: 916–929.

[5] Cheng XY, Yang X, Liu ML, *et al.* Preparation of ZrC coating in TRISO fuel particles by precise transportation of solid precursor and its microstructure evolution. *J Nucl Mater* 2023, **574**: 154222.

[6] Shih C, Tulenko JS, Baney RH. Low-temperature synthesis of silicon carbide inert matrix fuel through a polymer precursor route. *J Nucl Mater* 2011, **409**: 199–206.

[7] Katoh Y, Vasudevamurthy G, Nozawa T, *et al.* Properties of zirconium carbide for nuclear fuel applications. *J Nucl Mater* 2013, **441**: 718–742.

[8] Liu YX, Wang H, Hao JC, *et al.* Key materials for extreme high-temperature environments: Ultra-high-temperature ceramics and their composites. *Extreme Mater* 2025, **1**: 38–66.

[9] Zhang ZX, Guan YQ, Huang Q, *et al.* Insight of the microstructure evolution and performance enhancement of spinodal decomposition in (Ti,Zr)C composite carbide ceramics: Multiscale simulation and experimental investigation. *Acta Mater* 2025, **282**: 120487.

[10] Chen L, Wang YJ, Li YP, *et al.* Microstructural evolution, mechanical and thermal properties of TiC–ZrC–Cr_3C_2 composites. *Int J Refract Met H* 2019, **80**: 188–194.

[11] Liang LQ, Wei BX, Wang D, *et al.* Densification, microstructures, and mechanical properties of (Zr,Ti)(C,N) ceramics fabricated by spark plasma sintering. *J Eur Ceram Soc* 2022, **42**: 6445–6456.

[12] Zhang ZX, Zhang ZY, Chang GR, *et al.* Nitrogen-induced stacking fault energy reduction enables spinodal-decomposition-driven toughening in (Ti,Zr)C ceramics. *J Adv Ceram* 2025, **14**: 9221188.

[13] Peng Z, Cui YJ, Song JB, *et al.* The effect of nitrogen doping on the ablation resistance of zirconium carbide ceramics. *J Adv Ceram* 2025, **14**: 9221069.

[14] Wang YJ, Yao MY, Hu ZY, *et al.* Microstructure and mechanical properties of TiB_2–40 wt% TiC composites: Effects of adding a low-temperature hold prior to sintering at high temperatures. *Ceram Int* 2018, **44**: 23297–23300.

[15] Ormanci Ozturk O, Goller G. Spark plasma sintering and characterization of ZrC–TiB_2 composites. *Ceram Int* 2017, **43**: 8475–8481.

[16] Huo SJ, Wang YJ, Yao MY, *et al.* Reactive sintering behavior and enhanced densification of (Ti,Zr)B_2–(Zr,Ti)C composites. *J Eur Ceram Soc* 2020, **40**: 4373–4380.

[17] Kong QY, Huo SJ, Chen L, *et al.* Microstructure evolution, enhanced hardness and toughness in the solid-solution ceramic composite by reaction pressureless sintering of ZrB_2 and TiC powders. *Ceram Int* 2022, **48**: 17981–17986.

[18] Peng P, Liu JX, Xin XT, *et al.* Dual-phase medium-entropy diboride–carbide ceramics with metal element exchange during sintering. *J Adv Ceram* 2025, **14**: 9221007.

[19] Lun HL, Zeng Y, Xiong X, *et al.* Oxidation behavior of boron-containing (Zr,Ti)C_xB_y solid solution ceramics at 1600 °C in air. *J Adv Ceram* 2023, **12**: 1989–2002.

[20] Zhao J, Xue JX, Liu HT, *et al.* Zrc ceramics incorporated with different-sized SiC particles. *Adv Appl Ceram* 2018, **117**: 383–388.

[21] Li JP, Meng SH, Wang ZB, *et al.* Study on ZrC–20 vol.% SiC_w ultrahigh temperature ceramics by hot pressing. *Adv Mater Res* 2012, **557–559**: 772–775.

[22] Zhang MM, Wei BX, Wang D, *et al.* Novel (Zr,Ti)(C,N)–SiC ceramics via reactive hot-pressing at low temperature. *Ceram Int* 2022, **48**: 29641–29651.

[23] Wang LW, Wei BX, Zhang MM, *et al.* Oxidation behavior and kinetics of (Zr,Ti)(C,N)–SiC ceramics with enhanced oxidation resistance at 850 °C–950 °C. *J Mater Res Technol* 2023, **27**: 6744–6755.

[24] Wang Y, Liu Q, Zhang B, *et al.* Microstructure and mechanical behaviour of transient liquid phase spark plasma sintered B_4C–SiC–TiB_2 composites from a B_4C–$TiSi_2$ system. *Ceram Int* 2021, **47**: 10665–10671.

[25] Yuan XS, Wang ZK, Cai QM, *et al.* Microstructure and mechanical properties of (TiB_2–SiC)/B_4C composite ceramics using ($TiSi_2$ + C) as sintering aid. *Ceram Int* 2025, **51**: 61683–61691.
[26] Dudina DV, Mukherjee AK. Reactive spark plasma sintering: Successes and challenges of nanomaterial synthesis. *J Nanomater* 2013, **2013**: 625218.
[27] Wang LJ, Zhang JF, Jiang W. Recent development in reactive synthesis of nanostructured bulk materials by spark plasma sintering. *Int J Refract Met H* 2013, **39**: 103–112.
[28] Miranzo P, González-Julián J, Osendi MI, *et al.* Enhanced particle rearrangement during liquid phase spark plasma sintering of silicon nitride-based ceramics. *Ceram Int* 2011, **37**: 159–166.
[29] Whitehead AJ, Page TF. Fabrication and characterization of some novel reaction-bonded silicon carbide materials. *J Mater Sci* 1992, **27**: 839–852.
[30] Yaghobizadeh O, Sedghi A, Baharvandi HR. Investigation of the effect of various parameters on the amount and morphology of nano-laminate MAX phase in Cf–C–SiC–Ti_3SiC_2 composite. *Int J Refract Met H* 2018, **71**: 292–300.
[31] Wang Y, Zhang GH, Chou K. Preparation and oxidation characteristics of ZrC–ZrB_2 composite powders with different proportions. *Int J Min Met Mater* 2022, **29**: 521–528.
[32] Xiang MY, Gu JF, Ji W, *et al.* Reactive spark plasma sintering and mechanical properties of ZrB_2–SiC–ZrC composites from ZrC–B_4C–Si system. *Ceram Int* 2018, **44**: 8417–8422.
[33] Wei BX, Yao J, Wang LW, *et al.* Intra/inter-type SiC–Ti_3SiC_2 reinforced (Ti,Zr)C ceramics via multi-scale microstructure design. *J Eur Ceram Soc* 2025, **45**: 117713.
[34] Sarian S. Diffusion of 44Ti in TiC_x. *J Appl Phys* 1969, **40**: 3515–3520.
[35] Wang D, Zhang YN, Jiao YM, *et al.* Reactive spark plasma sintering of an electrically conductive B_4C–SiC–ZrB_2 composite with enhanced mechanical properties. *J Eur Ceram Soc* 2024, **44**: 2720–2729.
[36] Wang LW, Wei BX, Wang D, *et al.* Novel α/β SiC–(Ti,Nb)B_2 toughened (Ti,Nb)C-based composites with enhanced mechanical properties fabricated by *in situ* reactions sintering at low temperature. *Ceram Int* 2024, **50**: 46211–46226.
[37] Wei BX, Jiang W, Wang D, *et al.* Dual plate-like grains of (Ti,Zr)B_2 and W_2B_5 toughened solid solution composites fabricated via *in-situ* reaction spark plasma sintering of (Ti,W)C and ZrB_2 powders. *J Eur Ceram Soc* 2024, **44**: 6206–6222.
[38] Wei BX, Wang LW, Jiang W, *et al.* Design, preparation, and enhanced mechanical properties of novel plate-like grains toughened (Zr,Ti,W,Ta)C medium-entropy ceramics fabricated by *in-situ* reaction hot-pressing. *J Mater Res Technol* 2024, **31**: 2945–2960.
[39] Wang LW, Wei BX, Yao J, *et al.* Novel Ti_3SiC_2–(Ti,Zr)B_2 toughened (Ti,Zr)C-based composites with enhanced mechanical properties fabricated by dual *in situ* reactions hot-pressing at low temperature. *J Mater Res Technol* 2024, **30**: 8822–8840.
[40] Wang LW, Wei BX, Wang D, *et al.* (Ti,Ta)C–(Ti,Ta)B_2–SiC based ceramics with core–rim structure by *in-situ* reaction sintering at low temperature: Formation mechanism and enhanced mechanical properties. *J Mater Sci Technol* 2026, **246**: 167–186.
[41] Yao J, Wei BX, Hou QH, *et al.* Core–shell structure-designed TiC-based ceramics with synergistic strength-toughness via low-temperature *in-situ* reaction sintering. *Int J Refract Met H* 2025, **132**: 107276.
[42] Zhao RQ, Wei BX, Wang LW, *et al.* Reactive hot-pressing of ultrafine dual phase high-entropy (Ti,Zr,Hf,Nb,Ta)C–SiC ceramics with enhanced mechanical properties. *Ceram Int* 2025, **51**: 36511–36524.
[43] Wei BX, Gao YF, Wang LW, *et al.* Novel (Ti,W)C–SiC–WSi_2 ceramics fabricated via *in situ* reaction spark plasma sintering at 1600 °C. *Ceram Int* 2024, **50**: 14907–14918.
[44] Yang Y, Wei BX, Gao YF, *et al.* Multiphase design of (Ti,W,Ta)C–SiC–WSi_2 ceramics via *in-situ* reaction sintering: Microstructure–property relationships and high-temperature oxidation mechanisms. *Int J Refract Met H* 2026, **136**: 107579.
[45] Zhang J, Liu GH, Cui W, *et al.* Plastic deformation in silicon nitride ceramics via bond switching at coherent interfaces. *Science* 2022, **378**: 371–376.
[46] Xu MB, Liu XM, Lu H, *et al.* Increase of specific interfacial coherence in nanocrystalline ceramic–metal composites. *Compos Part B-Eng* 2023, **263**: 110873.
[47] Paterson MS. X-ray diffraction by face-centered cubic crystals with deformation faults. *J Appl Phys* 1952, **23**: 805–811.
[48] Zhang XY, Li B, Liu Q. Non-equilibrium basal stacking faults in hexagonal close-packed metals. *Acta Mater* 2015, **90**: 140–150.
[49] Wei BX, Wang YJ, Zhang HB, *et al.* Microstructure evolution of nonstoichiometric $ZrC_{0.6}$ with ordered carbon vacancies under ion irradiation. *Mater Lett* 2018, **228**: 254–257.
[50] Li Y, Katsui H, Goto T. Spark plasma sintering of TiC–ZrC composites. *Ceram Int* 2015, **41**: 7103–7108.
[51] Li Y, Katsui H, Goto T. Preparation of ZrCN–TiCN solid solutions by spark plasma sintering. *Ceram Int* 2017, **43**: 16965–16971.
[52] Feng L, Fahrenholtz WG, Hilmas GE, *et al.* Densification, microstructure, and mechanical properties of ZrC–SiC ceramics. *J Am Ceram Soc* 2019, **102**: 5786–5795.
[53] Ma B, Zhang X, Han J, *et al.* Microstructure and mechanical properties of ZrC–SiC–Cg ceramic prepared by hot pressing. *Rare Metal Mat Eng* 2009, **S2**: 890–893.
[54] Zhao LY, Jia DC, Duan XM, *et al.* Pressureless sintering of ZrC-based ceramics by enhancing powder sinterability. *Int J Refract Met H* 2011, **29**: 516–521.
[55] Kljajević L, Nenadović S, Nenadović M, *et al.* Spark plasma sintering of ZrC–SiC ceramics with $LiYO_2$ additive. *Ceram Int* 2013, **39**: 5467–5476.
[56] Feng L, Fahrenholtz WG, Hilmas GE. Effect of ZrB_2 content on the densification, microstructure, and mechanical properties of ZrC–SiC ceramics. *J Eur Ceram Soc* 2020, **40**: 220–225.
[57] Zhao LY, Jia DC, Duan XM, *et al.* Low temperature sintering of ZrC–SiC composite. *J Alloys Compd* 2011, **509**: 9816–9820.
[58] Vallauri D, Atías Adrián IC, Chrysanthou A. TiC–TiB_2 composites: A review of phase relationships, processing and properties. *J Eur Ceram Soc* 2008, **28**: 1697–1713.
[59] Warlimont H. Ceamics. In: *Springer Handbook of Condensed Matter and Materials Data*. Martienssen W, Warlimont H, Eds. Berlin: Springer, 2005: 462-463.
[60] Liu SZ, Hu YX, Ma JY, *et al.* Study of the microstructure, physical and mechanical properties of zirconium disilicide ceramics: Synthesis, experimental characterization and theoretical calculations. *Inorg Chem* 2025, **64**: 7110–7118.
[61] Wang HY, Xue FY, Zhao NH, *et al.* First-principles calculation of elastic properties of TiB_2 and ZrB_2. *Adv Mater Res* 2010, **150–151**: 40–43.
[62] Kiyashko MV, Grinchuk PS, Kuznetsova TA, *et al.* Determination of elastic modulus of SiC-based composite ceramics. *Tech Phys Lett+* 2021, **47**: 150–153.
[63] Xu BH, Zhang XD, Wang F. Mechanical properties, tensile strength, anisotropy and electronic properties of Zr_xSi_y intermetallics. *Chem Phys Lett* 2023, **833**: 140902.
[64] Sahin FC, Apak B, Akin I, *et al.* Spark plasma sintering of B_4C–SiC composites. *Solid State Sci* 2012, **14**: 1660–1663.
[65] Zhang ZW, Mei M, Li L, *et al.* Influence of ZrC on the microstructure of its surrounding resin-based carbon at high temperature. *New Carbon Mater* 2016, **31**: 451–454.
[66] Sadhasivam M, Jain VKS. Enhanced mechanical and thermal properties of AISI 420/TiB_2 composites fabricated by liquid metallurgy route. *Coll Compos Commun* 2021, **23**: 100550.
[67] Zhang XR, Zhang ZX, Wang WM, *et al.* Preparation of B_4C composites toughened by TiB_2–SiC agglomerates. *J Eur Ceram Soc* 2017, **37**: 865–869.
[68] Du XW, Zhang ZX, Wang WM, *et al.* Microstructure and properties of B_4C–SiC composites prepared by polycarbosilane-coating/B_4C powder route. *J Eur Ceram Soc* 2014, **34**: 1123–1129.
[69] Li ZJ, Guo RR, Li L, *et al.* Microstructure and fracture toughness of SiAlCN ceramics toughened by SiC_w or GNPs. *Ceram Int* 2023, **49**: 29709–29718.
[70] Ojalvo C, Moreno R, Guiberteau F, *et al.* Manufacturing B_4C parts with Ti–Al intermetallics by aqueous colloidal processing. *J Eur Ceram Soc* 2020, **40**: 226–233.